

## Quantification of effects of geometry of sediment bedrock interface on ground motion in 3D basin with circular free surface

*Jay Prakash Narayan and Kamal*

Department of Earthquake Engineering, Indian Institute of Technology Roorkee, India

*Received 20 November 2014, in final form 29 April 2015*

This paper presents the effects of geometry of sediment bedrock interface (GSBI) of 3D basins with a circular outcropping free surface on the characteristics and the focusing of the basin-generated surface (BGS) waves and associated spatial variations of the average spectral amplification (ASA) and average aggravation factor (AAF). An increase of ASA towards the centre of the semi-spherical (SS-) basin as compared to the 2D basin revealed the focusing of the BGS-waves in the SS-basin. The obtained 2.8 times larger ASA at the centre of the SS-basin to that of 2D basin calls for a special attention in predicting the seismic hazard in such basins for earthquake engineering purposes. The analysis of the simulated results revealed that the amplitude amplification due to the focusing of the BGS-waves was highly affected by the GSBI. For example, the ASA at the centre of a trapezoidal basin with edge slope  $20^\circ$  was 50% larger than that at the centre of a trapezoidal basin with edge slope  $45^\circ$ . It is recommended to compute the AAF using the same components of ground motion as that of the incident wave to conservatively aggravate the ground motion to incorporate the 3D basin-effects in the seismic microzonation where it is over based on the 1D response of sediment column.

*Keywords:* 3D viscoelastic finite-difference simulation, basin-generated surface waves, focusing of surface waves, aggravation factors and average spectral amplification

### 1. Introduction

The quantification of multi-dimensional 3D basin effects on the ground motion characteristics is very much essential for the seismic microzonation of an area, assessment of seismic risk and cost effective earthquake engineering (Chaljub et al., 2010). The multi-dimensional basin effects sometimes cause very peculiar damage pattern in basin. Some of the wave propagation phenomenon responsible for the peculiar damage are described in the following few sentences.

The physical phenomena like double-resonance caused unexpected and selective damages in Mexico city during the Mexico earthquake of 1985 and Ahmedabad city during Bhuj earthquake of 2001, India (Narayan et al., 2002; Kumar and Narayan, 2008a). The basin-generated surface (BGS) waves caused unexpected intense damage in a zone with some width and parallel to basin-edge during Northridge earthquake of 1994 and Kobe earthquake of 1995 (Kawase, 1996; Graves et al., 1998; Pitarka et al., 1998). The subsurface synclinal basement focusing of the incident body waves caused intense anomalous damage to only unreinforced brick chimneys in West Seattle, Washington during the 2001 Nisqually earthquake and very peculiar damage pattern in the Santa Monica area, Los Angeles basin during the Northridge earthquake of 1994 (Gao et al., 1996; Davis et al., 2000; Booth et al., 2004; Narayan and Kumar, 2012; 2014a). The focusing of body wave by the ridge-topography at the free surface causes complex ground motion amplification and de-amplification pattern along the ridge-flanks and a maximum amplification at the crest of the ridge (Geli et al., 1988; Narayan and Kumar, 2014b). Sometimes, complex mode transformation and amplification of the basin-transduced surface waves develops unexpected ground motion in the basins (Kawase, 1993; Narayan 2010; 2012).

Most of the recent simulations of the 3D basin responses were limited to comparing the simulated results with the earthquake records as well as to explain the occurred damage patterns in the basins (Dhakal and Yamanaka, 2013; Lee, 2013) using either no sediment-damping (Pitarka et al., 1998; Chavez-Garcia, 2003) or simple approaches without considering the separate sediment-damping for the P- and S-waves (Lee et al., 2008; Lee, 2013; Dhakal and Yamanaka, 2013). Based on the literature review, it appears that the role of geometry-of-sediment-bedrock-interface (GSBI) in the development and focusing of the BGS-waves and associated spatial variation of ground motion characteristics in a 3D basin remains unresolved. To study the effects of GSBI on the amplitude and focusing of the BGS-waves four basin models with different GSBI but a common circular free surface are considered. The maximum depth of sediment and other parameters were the same in all the considered basins. A circular free surface for all the basins is considered so that the focusing of the BGS-waves (an interesting wave propagation phenomenon) can be highlighted and analysed easily. The intracratonic basins and the basins formed due to the impact of a crater are generally circular in shape. Sometimes, certain geological phenomenon is also responsible for the development of basins with circular free surface. For example, the Chhattarpur basin with almost a circular free surface is developed in the outcropping Aravali formation in New Delhi, India. The subsurface geometry of the 3D basins is generally very complex. But, the simpler semi-spherical, conal and trapezoidal GSBI are considered to fulfill the aim.

In this paper, the effects of GSBI on the focusing of the BGS-waves in 3D basins with a common circular free surface and associated spatial variation of average spectral amplification (ASA) and average aggravation factor (AAF) is

documented (spectral aggravation factor is simply the extra spectral amplification due to the complex 2D or 3D basin effects over the 1D response in the respective basin and AAF is the average of spectral aggravation factors). The considered four SS-, CN-, TR45 and TR20-basin models have GSBI as semi-spherical (SS-basin), conal (CN-basin), trapezoidal with edge-slope  $45^\circ$  (TR45-basin) and trapezoidal with edge-slope  $20^\circ$  (TR20-basin), respectively. The seismic responses were computed using a 3D staggered-grid finite-difference (FD) algorithm capable of simulating the seismic response in the time-domain with frequency-dependent damping (Narayan and Sahar, 2014; Kamal and Narayan, 2015). The developed maps for the spatial variation of amplitude amplification, ASA and AAF in the basins are analyzed to infer the effects of GSBI on the amplitude and focusing of the BGS-waves. The wave-field snapshots at different times were also computed to infer the effects of GSBI on the characteristics of the BGS-waves and their focusing in basins.

## 2. Salient aspects of the used computer programs

The quantification of role of BGS-waves in the spatial variation of ASA and AAF in basin requires the incorporation of frequency-dependent damping in the time-domain simulations. The modified version of forth-order accurate 3D viscoelastic FD program of Narayan and Sahar (2014) for displacement-stress relation is used for the simulations. The frequency-dependent damping in the FD simulations is incorporated based on the GMB-EK rheological model. In the GMB-EK rheological model m-Maxwell bodies and one Hooke element are connected in parallel (Emmerich and Korn, 1987). Further, a material independent anelastic function developed by Kristek and Moczo (2003) is used since it is preferable in case of material discontinuities in the FD grid. The effective values of the unrelaxed Lamé's parameters and density at the desired location in the staggered-grid are obtained using the harmonic and arithmetic means, respectively to incorporate the material discontinuity (Moczo et al., 2002). The details of computation of unrelaxed moduli, anelastic coefficients and anelastic functions at four relaxation frequencies and the validation of incorporation of frequency dependent damping in the time domain FD algorithm are given in Narayan and Sahar (2014). In order to increase the speed of numerical computations, the programs was optimized and auto-parallelized using PGI Cuda-Fortran compiler. The VGR-stress imaging technique proposed by Narayan and Kumar (2008) is used as a free surface boundary condition. The sponge absorbing boundary condition is implemented on the model faces to avoid the edge reflections (Israeli and Orszag, 1981; Kumar and Narayan, 2008b).

## 3. 3D basin models

To study the effects of GSBI on the amplitude and focusing of the BGS-waves, the considered four basin models namely SS-basin, CN-basin, TR45-basin and

TR20-basin are shown in Fig. 1, a–d, respectively. As mentioned earlier, the intersection of these basins with the free surface is circular. The radius of circular free surface part of the basins is 5.0 km. The maximum depth of sediment (600 m) is same in all the basin models. The radius of curvature of the GBSI of the SS-basin is 21.13 km. Similarly, the TR45-basin and TR20-basin were incorporated into the model using an equation of semi-sphere with radius of curvature as 6.66 km and 14.04 km, respectively. The P- and S-waves velocities and the

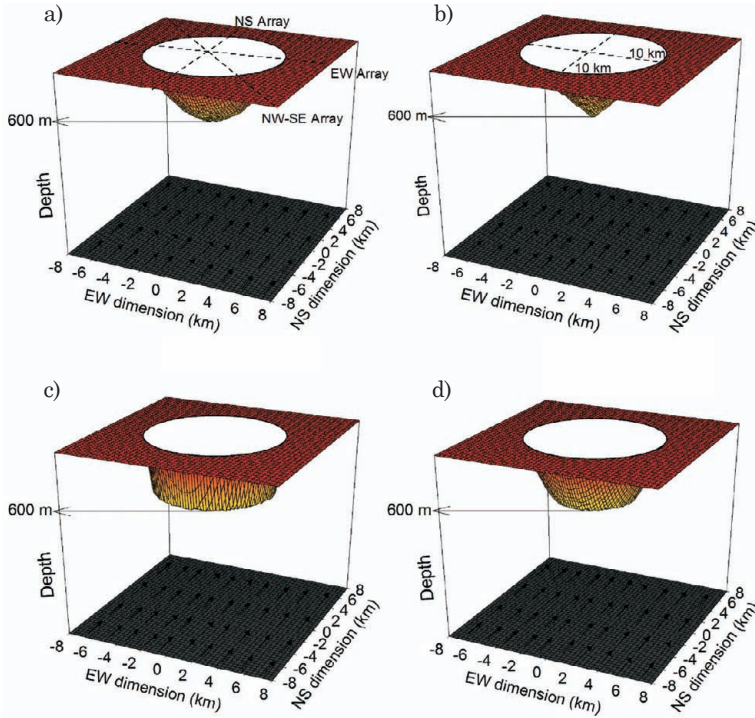


**Figure 1.** The vertically exaggerated SS-basin (a), CN-basin (b), TR45-basin (c) and TR20-basin models (d), respectively.

*Table 1. Rheological parameters for the SS, CN, TR45 and TR20 basin models.*

Rheology	Velocity at $F_R$ (m/s)		Density ( $\text{kg/m}^3$ )	$Q$ at $F_R$	Unrelaxed moduli (GPa)		
	S-wave	P-wave		$Q_P = Q_S$	$U$	$K_U$	$\lambda_U$
Sediment	650	1216	2000	65.00	0.884	3.094	1.326
Basement	2000	3460	2400	200.00	9.741	29.155	9.672

quality factors at a reference frequency ( $F_R=1.0$  Hz), densities and unrelaxed moduli for the sediment and basement rock are given in Tab. 1.

A plane S-wave front with NS (north-south) polarization was generated at depth of 1.08 km. The horizontal plane S-wave front is developed by using various point sources at a particular horizon. Further, to have a NS-polarization in the plane S-wave front, the point sources have been generated applying only  $\sigma_{ZX}$  shear stress at location of each point source in the form of Ricker wavelet (*Note: X, Y and Z coordinates are pointing towards north, west and vertically downward, respectively*). The used Ricker wavelet as a source excitation function has 1.0 Hz dominant frequency and considerable energy in the frequency range from 0.1 Hz to 2.5 Hz. Figure 2 shows the normalised Ricker wavelet and its spectra. A continuous-variable-grid-size in all the directions was used to reduce the need of both the computational memory and time. The horizontal grid size in X- and Y-directions in the computational zone was taken as 20 m and thereafter 100 m. Similarly, in the vertical direction, the grid size was 20 m up to depth of 1040 m and 100 m thereafter. The time step and lowest grid size were taken as 0.0032 s and 20 m to insure that the FD computation is free from the grid-dispersion and stability problems.

The seismic responses were computed on 15 east-west arrays (EWA1-EWA15) having 15 equidistant (0.8 km apart) receiver points (Fig. 3a). In other words, the seismic responses were computed at the 225 receiver points. The distance between two consecutive array was also 0.8 km. The R1-R15 receivers in EWA1-EWA15 arrays are extending 5.6 km east to 5.6 km west of a NS line passing through the centre of basins. It means, total area covered by the recording points was a square of size  $11.2 \times 11.2$  km. So, the study area is divided into  $15 \times 15$  square micro-zones (225) with dimension of 0.8 km. The depth of sediment below each receiver point in all the considered four basins were used to develop 1000 1D basin models. The seismic responses of all the 1000 1D basin models were used to compute the AAF at each receiver points. Three more arrays namely NS-, EW- and NW-SE passing through the centres of the SS-basin were considered as shown in Fig. 3. The EW-array is the same as EWA8 array. The NS-array contains R8 receivers of all the EWA1-EWA15 arrays. The wave-field snapshots were also computed to infer the effects of GSBI on the amplitude, focusing of the BGS-waves and their propagation.

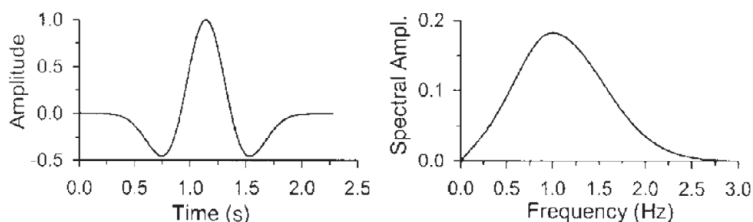


**Figure 2.** Ricker wavelet and its spectra, respectively.

#### 4. Seismic responses of the 2D basin and SS-basin

First to infer the effects of focusing of the BGS-waves on the ground motion in a 3D basin as compared with the 2D response of the same basin, the seismic responses of the SS-basins as well as its 2D section passing through the centre (referred as 2D basin in rest of the manuscript) along the NS-array were computed (Fig. 3b). The seismic responses of the 2D basin and SS-basin along the NS array for the NS polarization of the incident plane S-wave front are shown in the left and right panels of Fig. 4, respectively. Figure 4 depicts that the NS polarization of the incident S-wave has caused only Rayleigh waves in both the 2D basin and SS-basin along the NS-array, since there is no signal in the EW component of the response of the SS-basin.

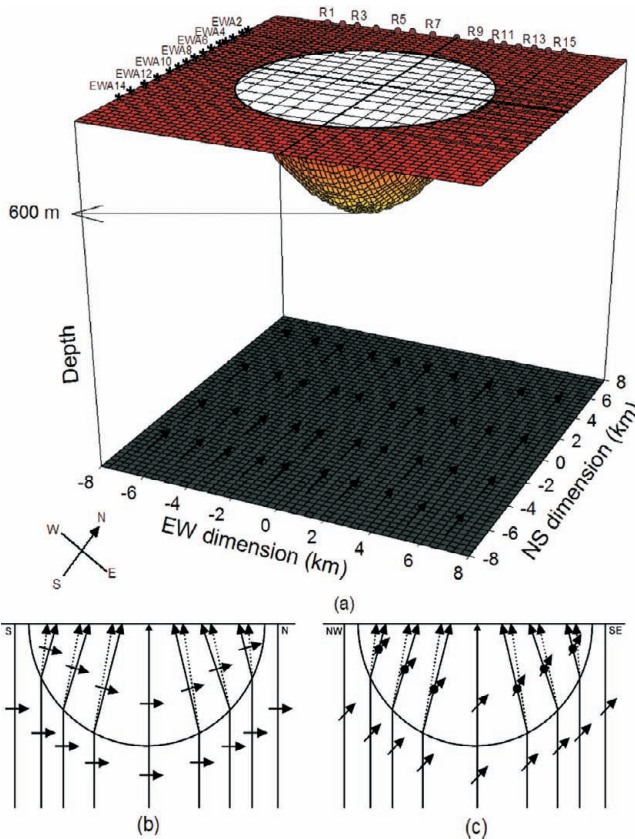


**Figure 3.** Fifteen EW-arrays and the NS-polarization of the vertically propagation plane S-wave front (a), NS-cross section passing through the centre of the SS-basin (b) and NW-SE cross section passing through the centre of the SS-basin (c).

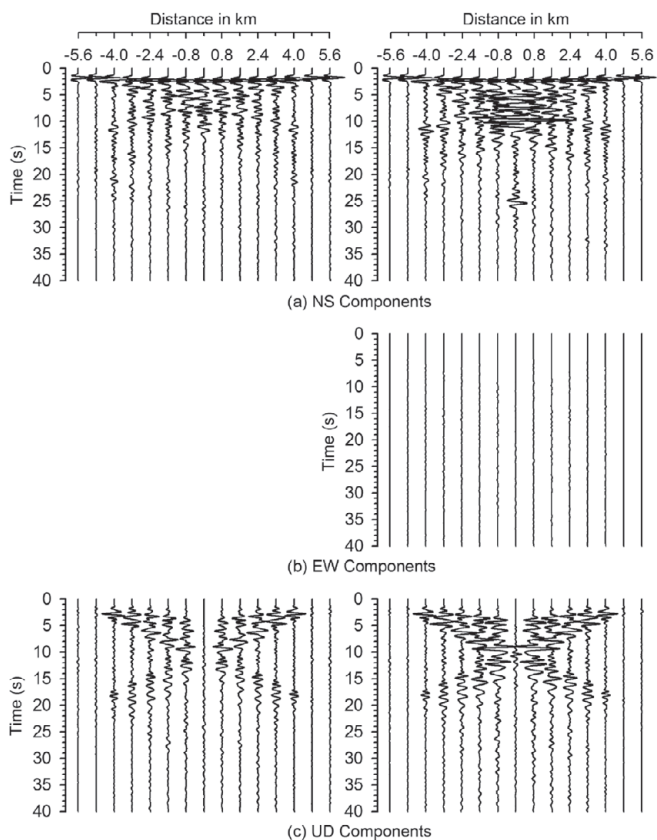


**Figure 4.** Seismic responses of the 2D basin (*left*) and SS-basin (*right*) along the NS-arrays.

In order to analyse Fig. 4, let us first discuss the mechanism behind generation of the BGS-waves in 2D basin and SS-basin. In case of 2D basin, as shown in Fig. 3b, the non-normal incidence of the S-wave at the synclinal interface between sediment and bedrock (NS elliptical plane) has caused the inclined transmitted S-wave towards the focus of the basin and the mode converted P-wave at each point along the synclinal interface, except the deepest point of the basin. The trapping and mode conversion of the transmitted S-wave in the basins has developed only Rayleigh waves (Bard and Bouchon, 1980a&b; Narayan, 2005). Similarly, it may be inferred that the NS-polarization of the incident S-wave will cause only Love wave in a semi-elliptical EW plane passing through the centre of the SS-basin since particle motion caused by the incident wave is transverse to the considered plane. In order to infer the type of surface waves generated in an infinite number of elliptical planes passing through the centre of the SS-basin, let us consider Fig. 3c which is an elliptical plane of the SS-basin oriented in NW-

SE direction. In the considered NW-SE elliptical plane, the components of the inclined transmitted S-wave may cause particle motion within the plane and transverse to the plane. Now, the trapping and the mode conversion at each reflection from the top and the bottom of the SS-basin may generate both the Love and Rayleigh waves in the considered NW-SE elliptical plane. Finally, it may be concluded that an incident S-wave may cause both the Rayleigh and Love waves which are propagating from each point along the periphery of the SS-basin towards the centre. However, the amplitudes of the generated Rayleigh and Love waves may depend on the amplitude of component of particle motion caused by the incident S-wave within and transverse to the plane of propagation, which is normal to the basin-edge. Now, a comparison of responses of the 2D basin and SS-basin reveals the tremendous increase of amplitude of the BGS-waves towards the centre of the SS-basin as compared to the 2D basin. The cause of increase of amplitude of the BGS-waves in the SS-basin is the focusing of the BGS-waves. On the other hand, minor increase of the amplitude of the BGS-waves in the horizontal component near the centre of the 2D basin may be attributed to the interference of the BGS-waves coming from opposite directions.

#### *4.1. Comparative ASA in the 2D basin and SS-basin*

A comparison of spatial variation of ASA in the NS and UD components of the 2D basin and SS-basin is shown in Fig. 5. The ASA is computed just by taking the average of spectral amplifications in the considered frequency band. The spectral amplifications were computed just by taking the ratio of spectra of the NS and UD components of ground motion in basins with the spectra of NS-component of ground motion recorded at the free surface of the respective models with no sediment. Figure 5 shows that the ASA near the edges of the 2D basin and SS-basin are comparable but the differences are increasing towards the centre of the basins in both the components. This reflects the effects of focusing of the BGS-waves in the SS-basin. The largest ASA in NS-component in the 2D basin and SS-basin are 2.15 and 6.14, respectively. Similarly, the largest ASA in UD-component in the 2D basin and SS-basin are 1.24 and 4.51, respectively. The ASA in the NS and UD components at the centre of the SS-basin are 2.8 and 2.6 times larger than at the centre of the 2D basin. It means, a tremendous increase of ground motion towards the centre of the SS-basin has occurred due to the focusing of the BGS-waves.

#### *4.2. Comparative AAF in the 2D basin and SS-basins*

2D and 3D AAF at different locations has been computed using the average of ratio of spectra of responses of the 2D basin and SS-basin with that of equivalent 1D basin at that particular location in the basins, respectively. Figure 5 also depicts the comparison of variation of AAF in the NS and UD components in the

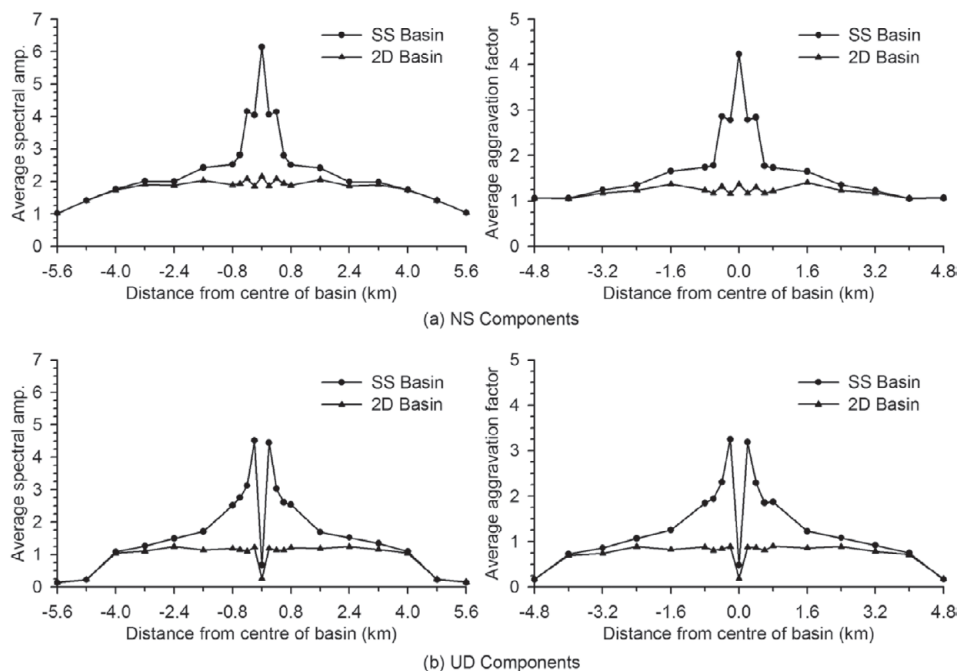


**Figure 5.** Comparisons of spatial variations of the ASA (*left*) and AAF (*right*) along the NS-arrays in the NS (*a*) and UD (*b*) components.

2D basin and SS-basin. The trend of spatial variation of AAF caused by the Rayleigh waves in the 2D basin and SS-basin are similar to the ASA. AAF in the NS and UD components at the centre of the SS-basin is 3.1 and 2.5 times larger than at the centre of the 2D basin. This finding calls for the special attention during the computation of ground motion amplification in the SS-basin for seismic hazard analysis.

## 5. Effects of GSBI

### 5.1. Seismic responses

The NS, EW and UD components of the seismic responses of the SS-basin on the EWA4, EWA6 and EWA8 linear seismic arrays are shown in Fig. 6. The EWA4, EWA6 and EWA8 arrays are at a distance of 3.2 km, 1.6 km and 0.0 km north of the centre of SS-basin, respectively. The NS components along the EWA4 array depicts very clearly the incident S-wave as first arrival and mainly Love waves generated at the western and the eastern edges of the SS-basin as the second and the third arrivals, respectively. The basin-generated Rayleigh

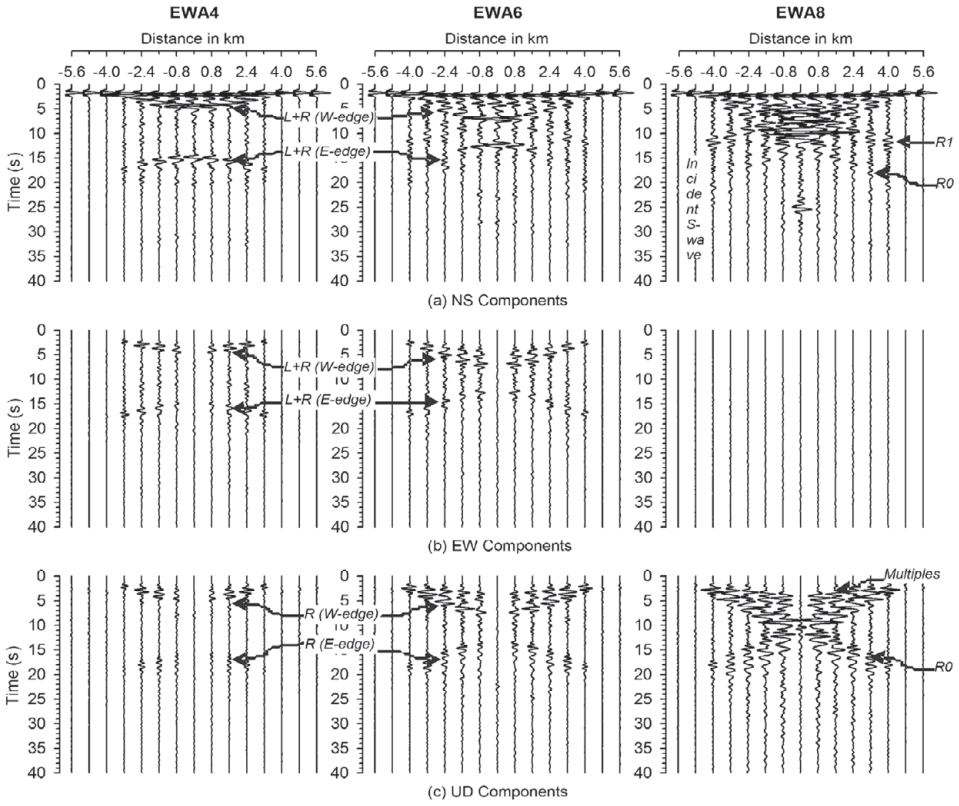


**Figure 6.** The NS (a), EW (b) and UD (c) components of the seismic responses of the SS-basin along the EWA4, EWA6 and EWA8 seismic arrays. (Note: L, R, R0, R1, W-edge and E-edge denote Love-wave, Rayleigh-wave, fundamental mode of Rayleigh wave, first mode of Rayleigh wave, western-edge of basin and eastern edge of basin, respectively.)

waves with very small amplitude are also tailing the Love waves. The large arrival time of the third arrival of Love waves is due to larger distance of southern edge of the SS-basin from the EWA4 array.

Similarly, the UD components along the EWA4 array in the SS-basin depicts very clearly the UD component of the incident S-wave as first arrival and basin generated Rayleigh waves at the western and eastern edges of the SS-basin as second and the third arrivals, respectively. The EW component depicts the recording of both the Love and Rayleigh waves generated at the western and the eastern edges of the SS-basin. Similar effects can be seen along the EWA6 array in the SS-basin with an increased contribution of the Rayleigh waves and body wave multiples. The signal recorded on NS and UD components along the EWA8

array depict the body wave and its multiples and basin generated Rayleigh waves, except 8<sup>th</sup> receiver of the NS component, where both the Love and Rayleigh waves have been recorded. The almost negligible amplitude in the UD component at the 8<sup>th</sup> receiver point of the EWA4, EWA6 and EWA8 arrays depicts that the polarities of the Rayleigh waves generated at the western edges are opposite to that on the eastern edges of the SS-basin. Responses of the CN-, TR45- and TR20-basins, shown in Figs. 7, 8 and 9 respectively, exhibit similar trend of recording along the EWA4, EWA6 and EWA8 seismic arrays. However, the ground motion characteristics are highly variable from one basin to another basin. Figures 6 to 10 illustrate an increase of amplitude of the BGS-waves towards the centre of basins due to the focusing of the BGS-waves.

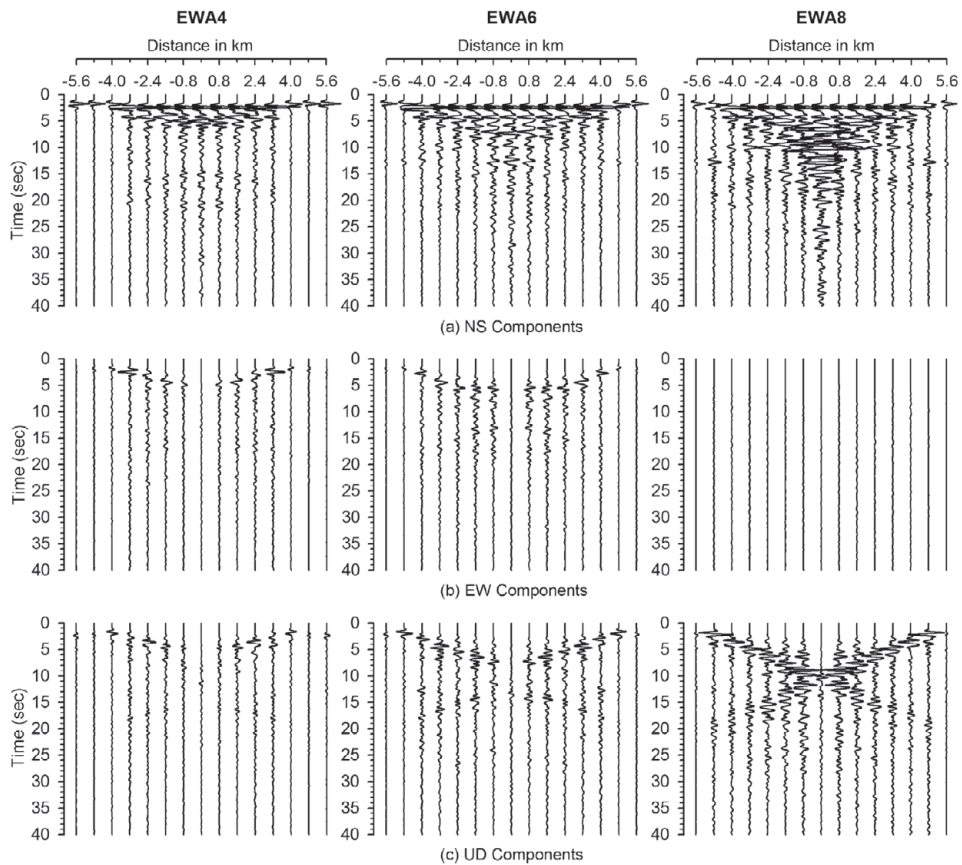


**Figure 7.** The NS (a), EW (b) and UD (c) components of the seismic responses of the CN-basin along the EWA4, EWA6 and EWA8 seismic arrays.

A comparison of ground motion recorded in the NS components at the centres of the SS-, CN-, TR45- and TR20-basins is shown in Fig. 10 (left panels). The analysis of these records depicts that the maximum amplitude in the trace was largest in TR20-basin (18.8 mm) and lowest in the CN-basin (9.0 mm). A comparison of spectral amplifications of the NS components at the centres of the SS-, CN-, TR45- and TR20-basins is also shown in Fig. 10 (right panels). The largest spectral amplifications at the centre of the SS-, CN-, TR45- and TR20-basins are 14.0, 16.1, 16.2 and 22.1, respectively. The largest spectral amplification in the TR20-basin is around 36% more than in the TR45-basin. However, frequencies corresponding to the largest spectral amplifications have no specific trend. This finding reflects that the ground motion characteristics at the centres of the basins are highly dependent on the GSBI.

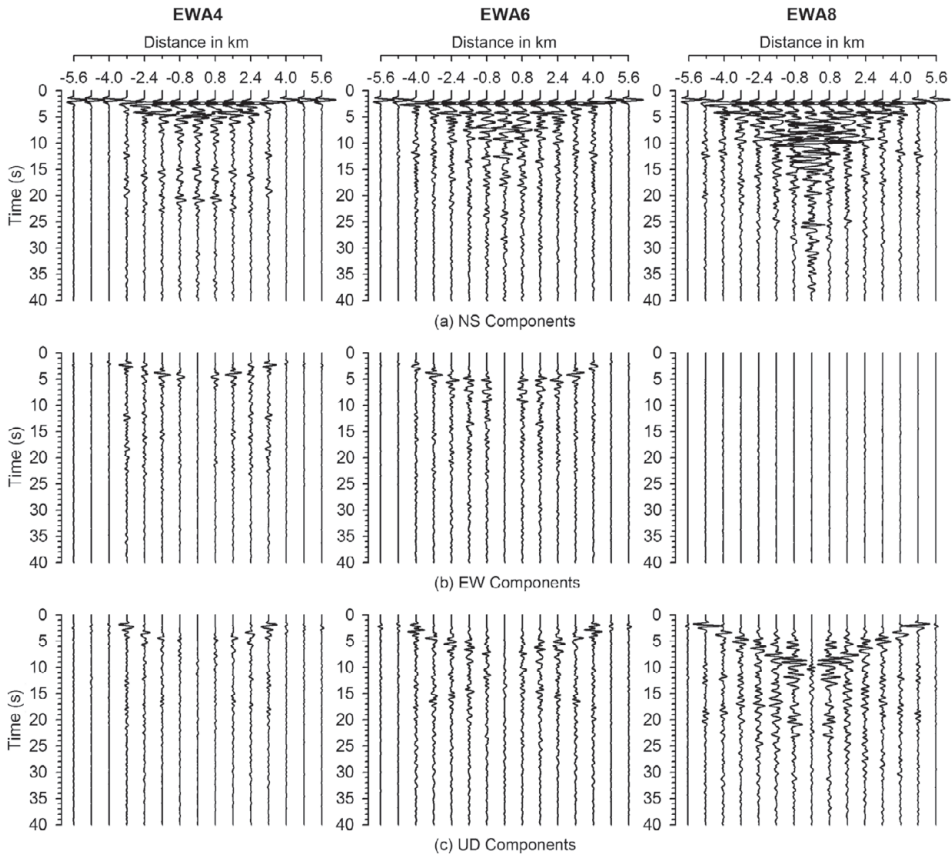


**Figure 8.** The NS (a), EW (b) and UD (c) components of the seismic responses of the TR45-basin along the EWA4, EWA6 and EWA8 seismic arrays.

### 5.2. Wave-field snapshots

In order to further demonstrate the effects of GBSI on the amplitude and focusing of the BGS-waves in the basins, the computed snapshots of the EW component at different times on the free surface are shown in Fig. 11. The wave-field snapshots of the EW component are chosen since it contains only the horizontal components of the BGS-waves and not the body wave components. The wave-field snapshots were computed in an area extending from 6.0 km south to 6.0 km north and 6.0 km west to 6.0 km east of the centre of the considered basins. The wave-field snapshot of the EW component at time 3.2 s shows the developed BGS-waves and their propagation towards the centre of the considered basins. An effect of GBSI on the amplitude of the BGS-waves can be inferred. The amplitude of the BGS-waves is largest in TR20-basin and smallest in the

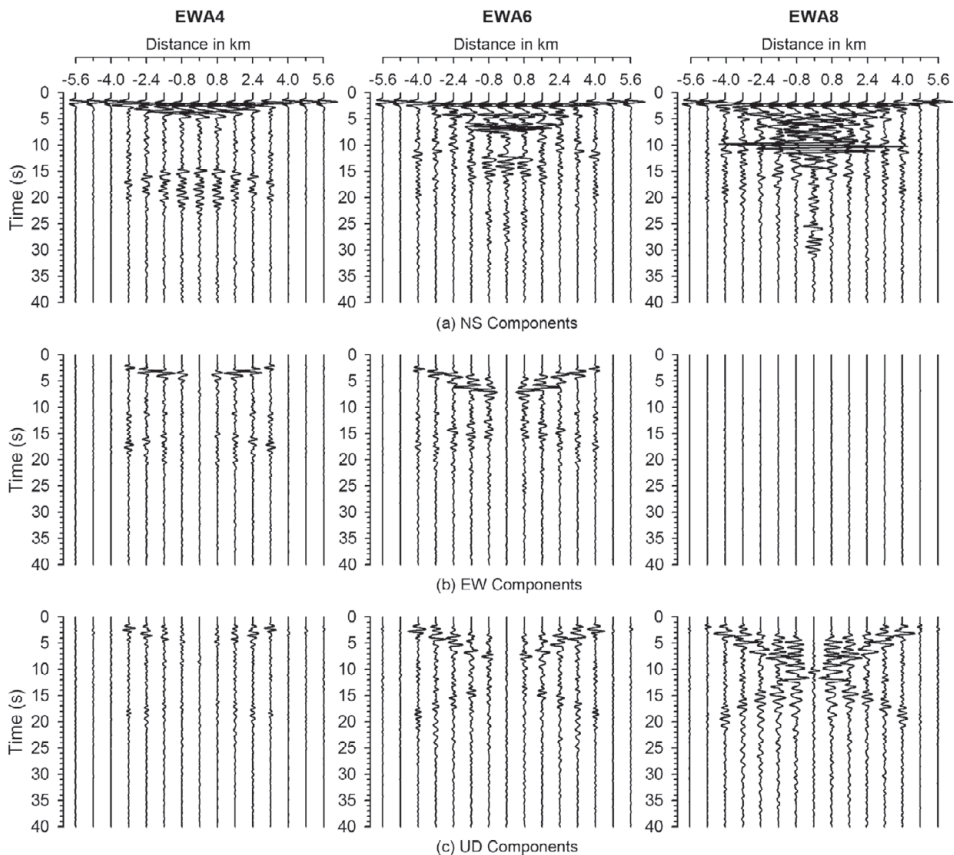


**Figure 9.** The NS (a), EW (b) and UD (c) components of the seismic responses of the TR20-basin along the EWA4, EWA6 and EWA8 seismic arrays.

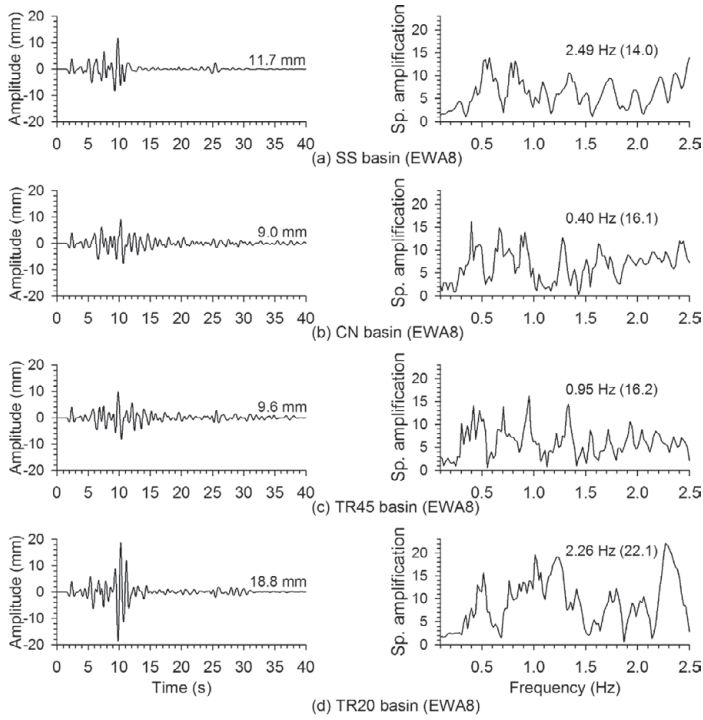


**Figure 10.** NS components of seismic responses and spectral amplifications at the centers of the SS-, CN-, TR4-5 and TR20-basins (*a-d*, respectively).

TR45-basin. An increase of amplitude and decrease of wave-front size of the BGS-waves can be inferred in the snapshots at times 5.6 s, 8.0 s and 10.4 s due to the BGS-wave focusing. An increase of duration of the BGS-waves with increase of travelled distance can also be inferred due to the dispersion of the BGS-waves. Very large amplitude in the wave-field snapshots at time 10.4 s reveals the effect of focusing of the BGS-waves, which has overtaken the effects of sediment-damping and the dispersion of the BGS-wave. A decrease of amplitude of the BGS-waves in the wave-field snapshots at time 12.8 s depicts the de-focusing of the BGS-waves.

### 5.3. Ground motion amplification

A comparison of spatial variation of the amplitude amplifications in the NS, EW and UD components in the SS-, CN-, TR45- and TR20-basins is shown in Fig. 12. The amplitude amplification is computed using the ratio of largest amplitude in different components recorded in the basins with the largest amplitude in the NS-component of a model containing no sediment. The amplitude ampli-

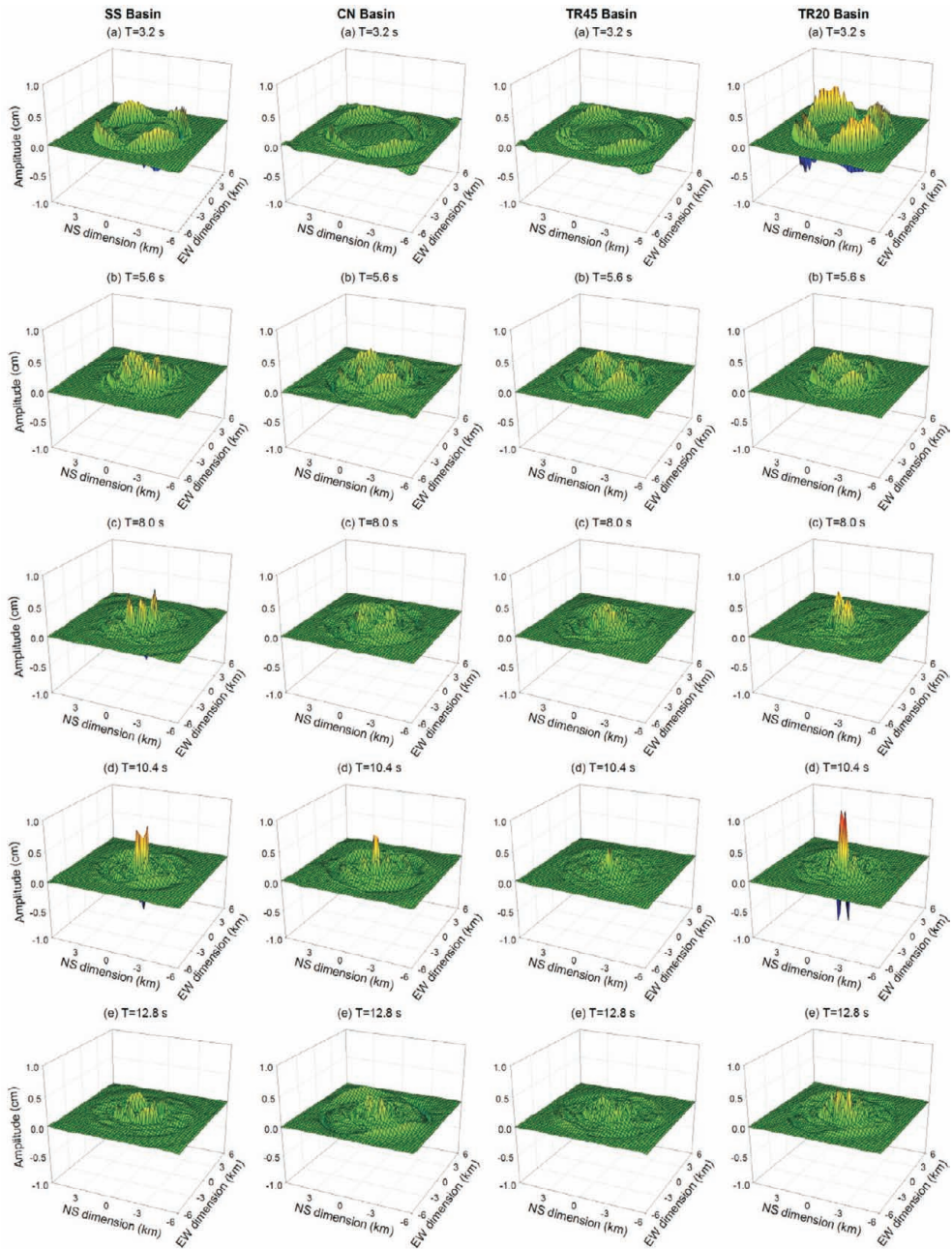


**Figure 11.** Wave-field snapshots of the EW components of responses of the SS-, CN-, TR45- and TR20-basins at different times.

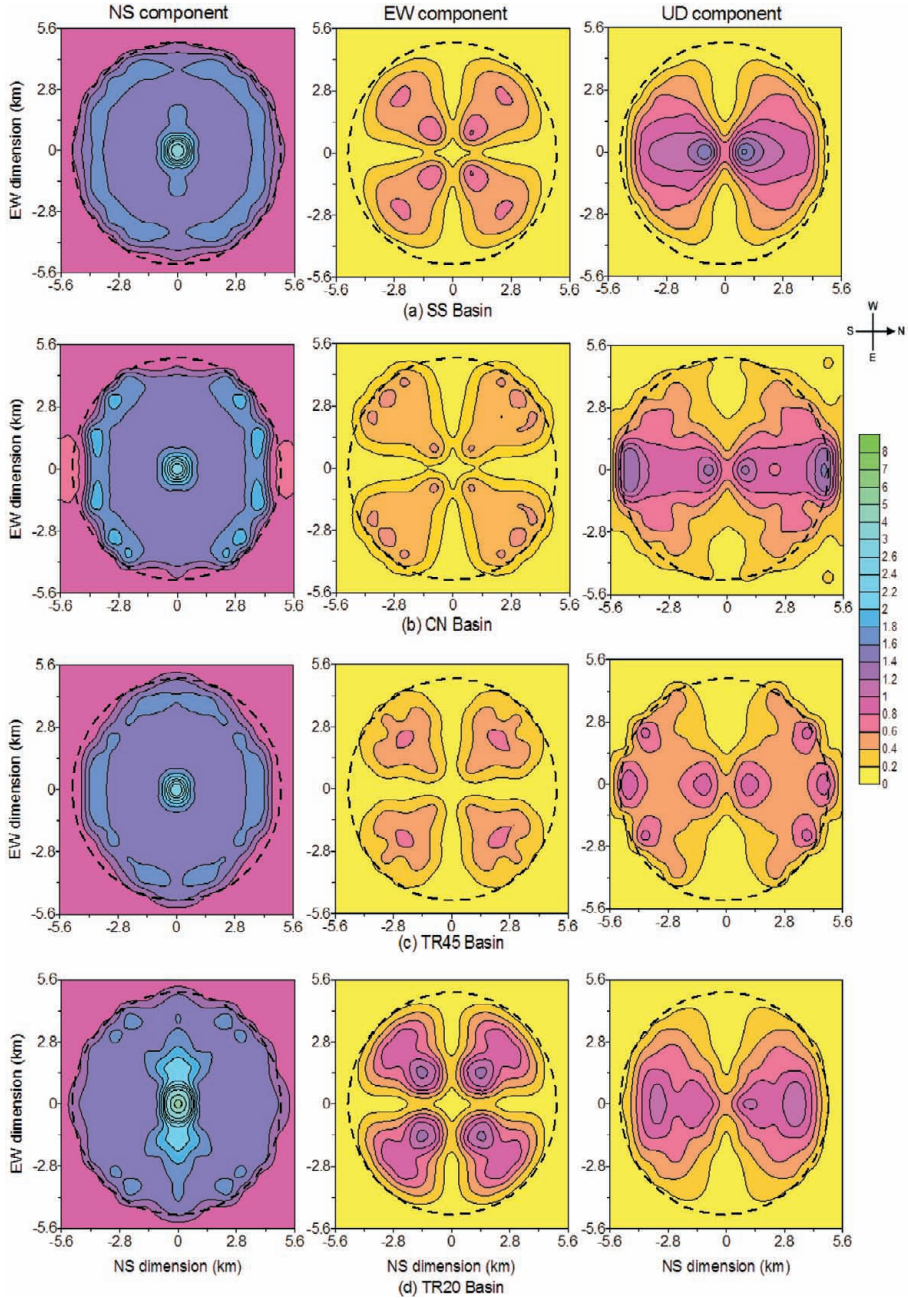


**Figure 12.** The spatial variation of amplitude amplification in the NS, EW and UD components in the SS- (a), CN- (b), TR45- (c) and TR20-basins (d), respectively. (Note: the number of contours are the same in the EW and UD components and lesser than in the NS components.)

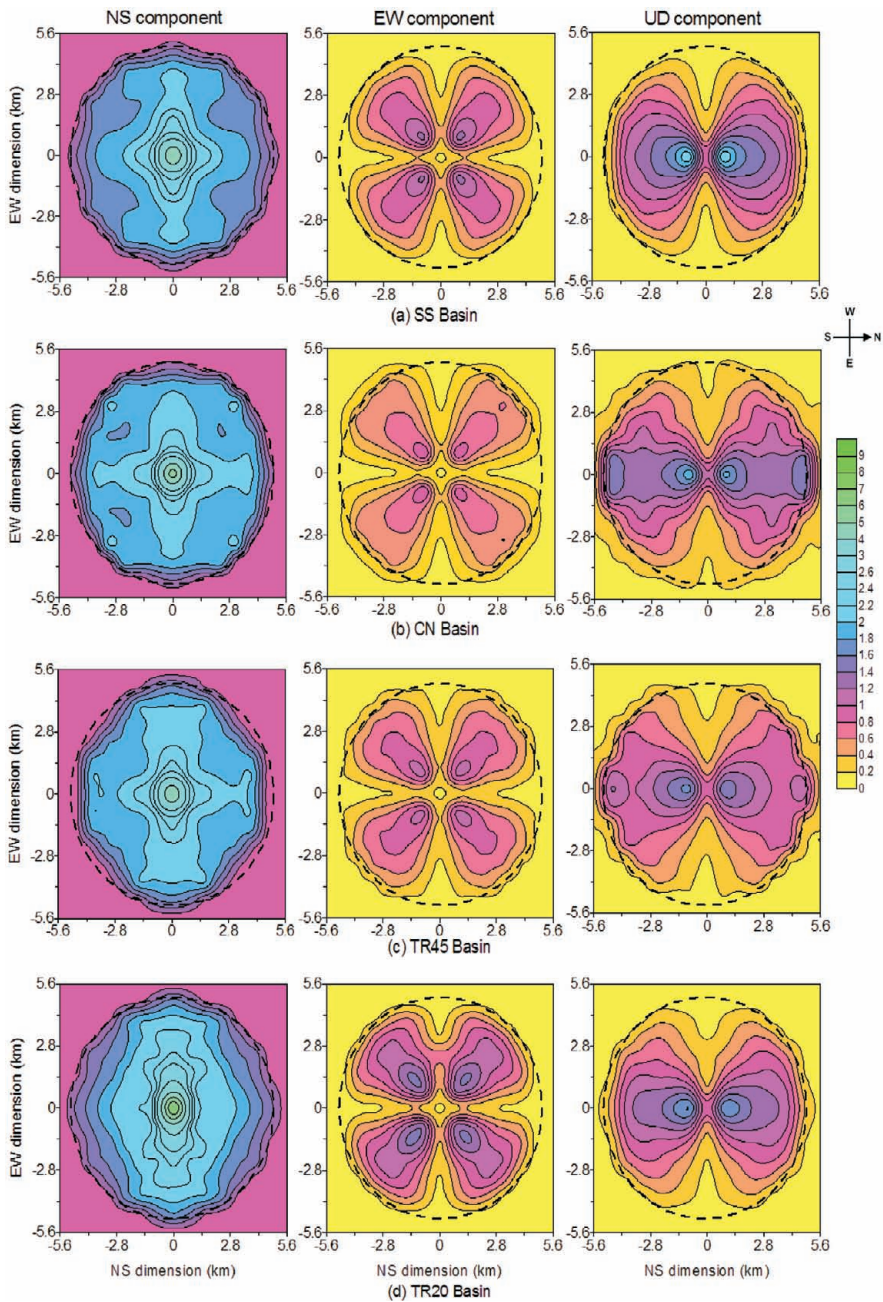


**Figure 13.** The spatial variation of ASA in the NS, EW and UD components in the SS- (a), CN- (b), TR45- (c) and TR20-basins (d), respectively.

fication in the NS-component has increased from around 1.0 near the edge to 4.52, 3.56, 3.62 and 7.25 at the centres of the SS-, CN-, TR45- and TR20-basins, respectively. Near the basin-edges, the amplitude amplification is governed by the amplitude of the incident S-waves but in the central part (1.5 km in diameter) it is governed by the amplitude of the BGS-waves. The amplitude amplification in the EW-components in the SS-, CN-, TR45- and TR20-basins have increased from negligible value near the edge to 1.03, 0.91, 0.75 and 1.33, respectively near the centres of the basins. Similarly, the amplitude amplification in the UD-components in the SS-, CN-, TR45- and TR20-basins have increased from negligible value near the edge to 1.95, 1.58, 1.18 and 1.20, respectively. The analysis of pattern of amplitude amplifications in the basins depicts that the amplitude of the BGS-waves is highly dependent on the GSBI. It can also be inferred that the amplitude of the Rayleigh waves in the UD component near the centre of basin is more in the SS- and CN-basins as compared to the trapezoidal basins. However, the amplitude of the Rayleigh waves in the UD component near the edge in the CN and TR20 basins is more than that in the SS- and TR45-basins.

A comparison of spatial variation of ASA in the NS, EW and UD components in the SS-, CN-, TR45- and TR20-basins is shown in Fig. 13. Figure 13 reveals that the largest ASA in the NS components of the SS-, CN-, TR45- and TR20-basins are of the order of 6.14, 6.71, 5.98 and 8.97, respectively at the centre of basins. Similarly, the largest ASA in the EW and UD components of the SS-, CN-, TR45- and TR20-basin are of the order of 1.54, 1.53, 1.31 and 1.63 as well as 2.54, 2.22, 1.85 and 2.04, respectively at the centre of basins. ASA in the UD components are mainly due to the basin generated Rayleigh waves. The ASA near the edges of all the basins in the respective components were comparable but the differences are increasing towards the centre of the basins due to effects of GSBI on the amplitude and focusing of the BGS-waves. Further, a comparison of ASA variation in the NS components in different basins along the NS-, EW- and NW-SE-arrays passing through the centre of basins depicts that the ASA is largest along an array where the Love wave propagates (Fig. 14). An analysis of Fig. 14 depicts that the vertical component of Rayleigh wave is more affected by the GSBI as compared to the horizontal component. The ASA in the EW components along the NW-SE direction, shown in left panel of Fig. 16, also reflects that the characteristics of the BGS-waves are very much dependent on the GSBI.

#### 5.4. Average aggravation factors

A comparison of spatial variation of AAF in the NS, EW and UD components in the SS-, CN-, TR45- and TR20-basins is shown in Fig. 15. The analysis of Fig. 15 depicts that the AAF is also largest in the NS components and least in the EW components of all the considered basins. A comparison of AAF variation in the NS components along the NS-, EW- and NE-SW-arrays passing through the centre of basins is shown in Fig. 14 (right). The largest AAF in the NS compo-

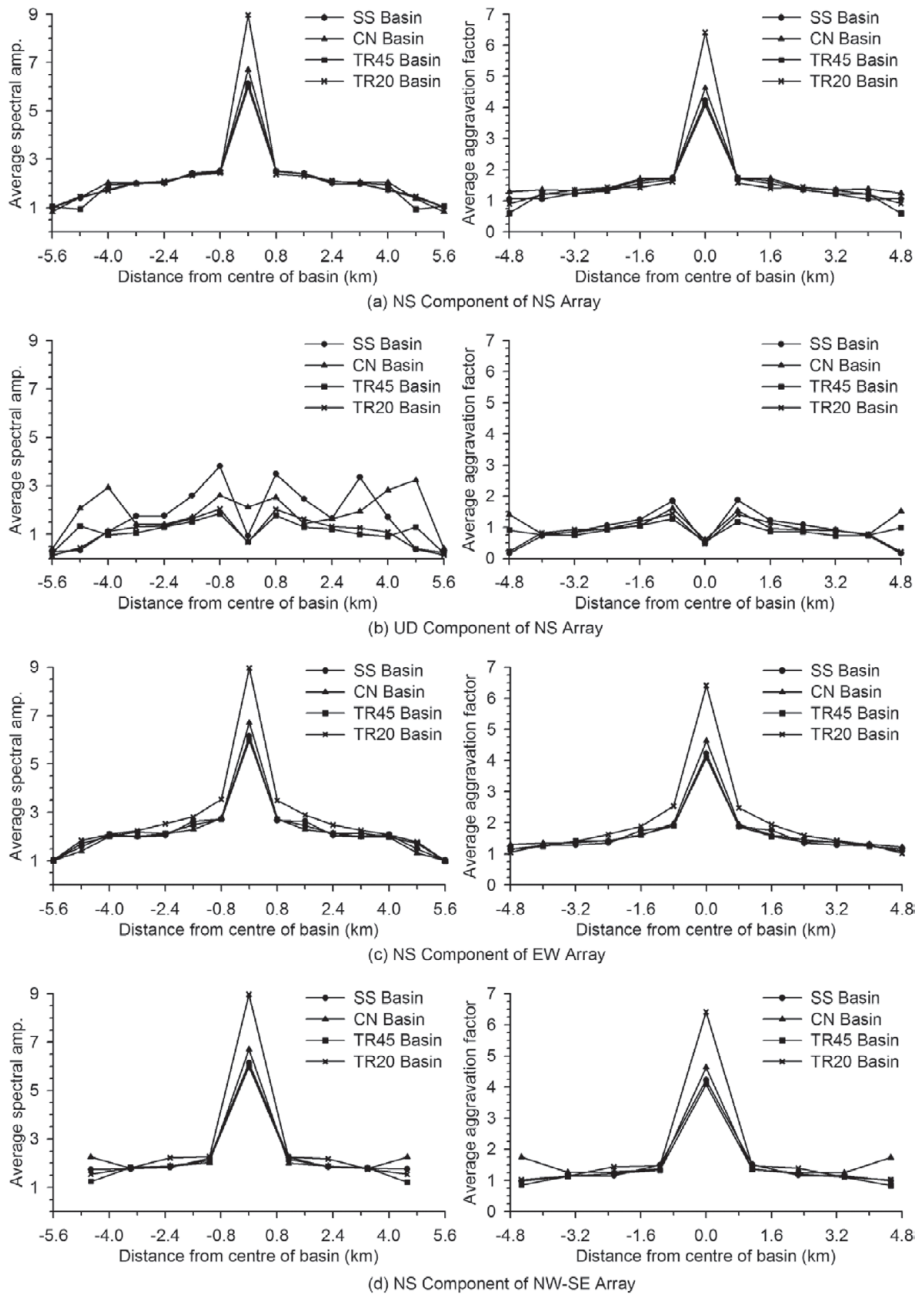


**Figure 14.** The spatial variation of ASA (*left*) and AAF (*right*) in the NS and UD components along the NS array (*a* and *b*) and NS components along the EW (*c*) and NE-SW (*d*) arrays passing through the centre of basins, respectively in the considered basin models.

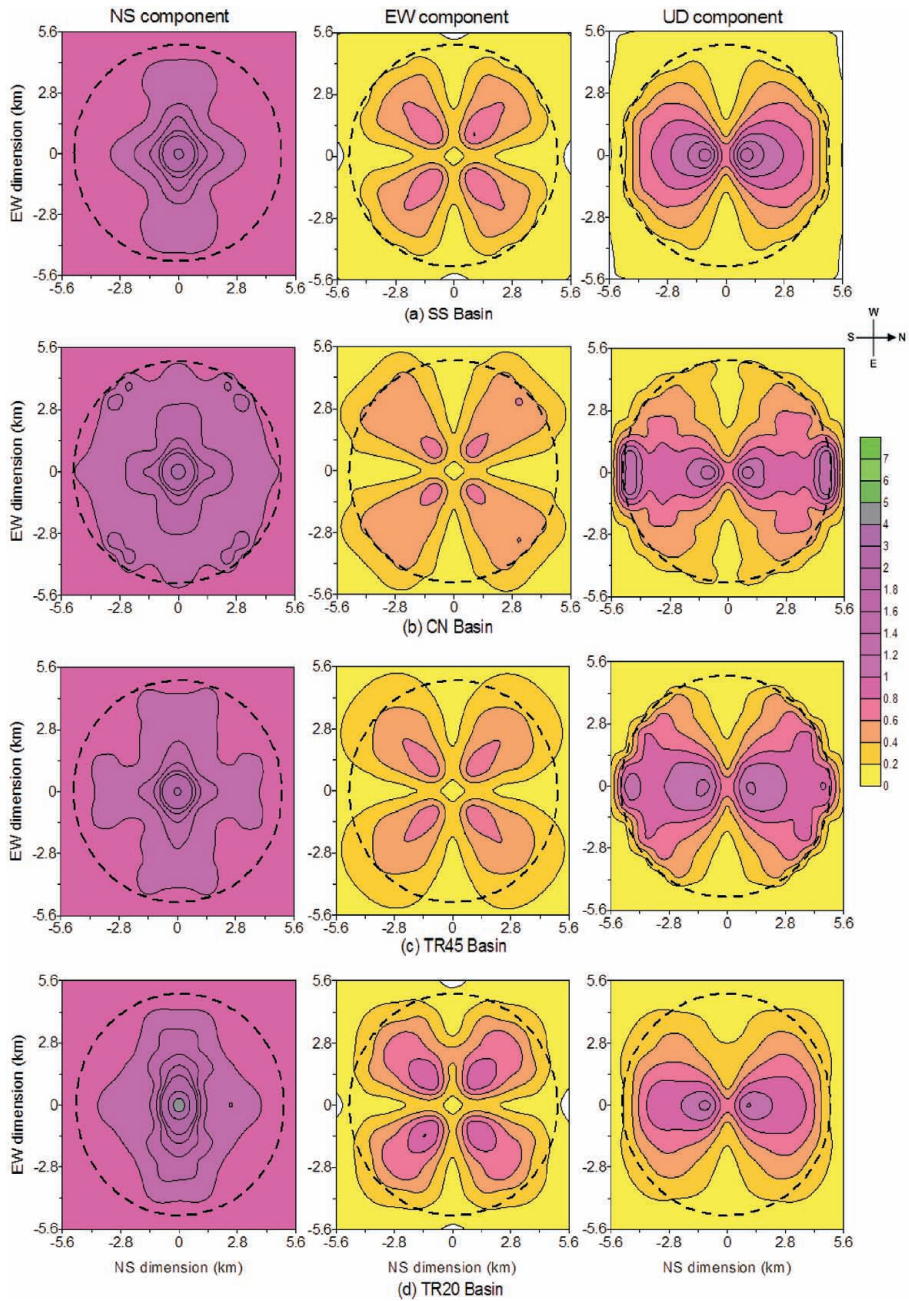


**Figure 15.** The spatial variation of AAF in the NS, EW and UD components in the SS-, CN-, TR45- and TR20-basins (*a-d*, respectively).

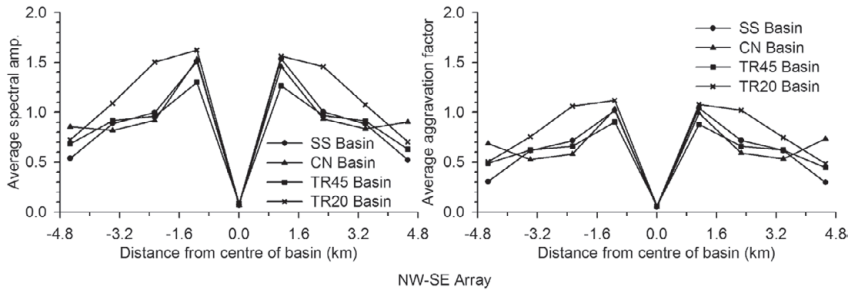


**Figure 16.** The spatial variation of ASA (*left*) and AAF (*right*) in the EW components in the considered basin models along the NE-SW array, passing through the centre of basins.

nents at the centres of the SS-, CN-, TR45- and TR20-basins were of the order of 4.23, 4.63, 4.09 and 6.42, respectively. Again, the analysis of spatial variation of AAF along the different arrays depicts that the AAF is larger along the array in which Love wave propagates. The AAF near the basin-edge in the UD component is largest in the CN-basin and least in the SS-/TR20-basins.

## 6. Discussion

It is of general acceptance that the area of slant part of basin-edge play main role in the forced trapping of body waves in basins and the development of the BGS-waves (Bard and Bouchon, 1980a&b; Narayan, 2005). The GSBI of the considered basins reflects that the decreasing order of trapped body waves energy in basins is  $CN > SS > TR20 > TR45$ . It can also be inferred that the decreasing size of wave-front or the focusing effects of the BGS-waves can be  $TR45 > TR20 > SS > CN$ . The basin in which trapping of body waves is over earlier means earlier BGS-waves generation and larger size of surface waves' wave front. Furthermore, the effects of sediment-damping on the BGS-waves in a decreasing order may be  $TR45 > TR20 > SS > CN$ . The increase of ASA towards the centre of the basins is favored by the focusing of the BGS-waves and trapped body wave energy and opposed by the sediment-damping. A comparison of level of ASA at the centers of TR45 (5.98) and R20 (8.97) basins reveals that the effect of longer length of slant part of basin bottom has overtaken the focusing effects of the BGS-waves. A comparison of level of ASA at the centers of CN (6.71) and SS (6.14) basins also corroborates with the above inference. But, a comparison of level of ASA at the centres of the TR20 and CN/SS-basins reveals that the effect of longer length of slant part of basin bottom has been overtaken by the focusing effects of the BGS-waves. So, to give a general solution to predict the complex effects of sediment-damping, BGS-wave focusing and GSBI on the amplitude of BGS-waves is not possible. However, it may be concluded that the GSBI plays a major role in the development and focusing of the BGS-waves.

Generally, the damage surveys and numerical simulations reveal that the BGS- waves cause intense damage in a bandwidth parallel to and at some distance from the out-cropping basin-edge (Pitarka et al., 1998; Narayan, 2005; Hallier et al., 2008). But, the obtained level of spatial variation of the ASA in the considered circular basins depicts that an unexpected damage may occur in the central part of basin and least damage near the basin-edge. The analysis of spatial variation of the AAF in the NS, EW and UD components along different arrays reveals that it is largest in the NS components since the polarization of the incident wave is also the NS-direction. Further, it is more along an array where only Love wave is recorded. As we know that in the current seismic microzonation procedure, the AAF is the only parameter to incorporate the 2D/3D site effects in seismic microzonation where it is over based on the 1D response (Chavez-Garcia and Faccioli, 2000; Sheuly and Narayan, 2012). So, it may be recommended conservatively that the AAF obtained in the same component as that of polarization of the used source should be used to aggravate the ground motion in order to incorporate the 3D basin-effects in the seismic microzonation.

## 7. Conclusions

The aim of this paper was to study the role of GSBI in development and focusing of the BGS-waves and associated spatial variation of ground motion in the 3D considered basins. A comparison of spatial variation of the obtained ASA in the 2D basin and SS-basin revealed that the 2D response of a 3D basin is totally inadequate since ASA at the centre of the SS-basin is more than 2.5 times to that at the centre of the 2D basin. This unexpected difference in ASA level may be mainly due to the focusing of the BGS-waves in the SS-basin. Further, the obtained level of ASA/AAF in the central part of the considered basins calls for a special attention during seismic hazard assessment in a basin whose surface area is circular. In contrast to this, in most of the basins, the BGS- waves cause intense damage near the basin-edge (Pitarka et al., 1998; Hallier et al., 2008; Narayan, 2005).

Based on the analysis of results and wave-field snapshots, it is inferred that the spatial variation of ASA/AAF in the considered basins was controlled by the GSBI, focusing of the BGS-waves and sediment-damping. However, the GSBI played major role in controlling the amplitude of the BGS-waves. For example, the obtained ASA at the centre of the TR20-basin was around 50% larger than that at the centre of the TR45-basin. The obtained level of AAF in the considered 3D basins clearly revealed the inadequacy of the 1D/2D approaches in predicting the transfer function of such a 3D basins (Chavez-Garcia and Faccioli, 2000). So, it is recommended to compute the AAF using the same component of ground motion as that of the incident body wave to conservatively aggravate the ground motion to incorporate the 3D basin-effects in the seismic microzonation where it has already been carried out using 1D response of the soil column.

## References

- Bard, P. Y. and Bouchon, M. (1980a): The seismic response of sediment filled valleys, Part 1. The case of incident SH-waves, *Bull. Seismol. Soc. Am.*, **70**, 1263–1286.
- Bard, P. Y. and Bouchon, M. (1980b): The seismic response of sediment filled valleys. Part 2. The case of incident P and SV-waves, *Bull. Seismol. Soc. Am.*, **70**, 1921–1941.
- Booth, D. B., Wells, R. E. and Givler, R. W. (2004): Chimney damage in the greater Seattle area from the Nisqually earthquake of 28 February 2001, *Bull. Seismol. Soc. Am.*, **94**, 1143–1159.
- Chaljub, E., Moczo, P., Tsuno, S., Bard, P. Y., Kristek, J., Kaser, M., Stupazzini, M. and Kristekova, M. (2010): Quantitative comparison of four numerical predictions of 3D ground motion in the Grenoble Valley, France, *Bull. Seismol. Soc. Am.*, **100**, 1427–1455, DOI: [10.1785/0120090052](https://doi.org/10.1785/0120090052).
- Chavez-Garcia, F. J. and Faccioli, E. (2000): Complex site-effect and building code: making the leap, *J. Seismol.*, **4**, 23–40, DOI: [10.1023/A:1009830201929](https://doi.org/10.1023/A:1009830201929).
- Chavez-Garcia, F. J. (2003): Site effects in Parkway basin: comparison between observations and 3D modelling, *Geophys. J. Int.*, **154**, 633–646, DOI: [10.1046/j.1365-246X.2003.02055.x](https://doi.org/10.1046/j.1365-246X.2003.02055.x).
- Davis, P. M., Justin, L., Rubinstein, K. H., Liu, S. S. and Knopoff, G. L. (2000): Northridge earthquake damage caused by geologic focusing of seismic waves, *Science*, **289**, 1746–1750, DOI: [10.1126/science.289.5485.1746](https://doi.org/10.1126/science.289.5485.1746).
- Dhakal, Y. P. and Yamanaka, H. (2013): An evaluation of 3-D velocity models of the Kanto basin for long-period ground motion simulations, *J. Seismol.*, **17**, DOI: [10.1007/s10950-013-9373-4](https://doi.org/10.1007/s10950-013-9373-4).
- Emmerich, H. and Korn, M. (1987): Incorporation of attenuation into time domain computations of seismic wave fields, *Geophysics*, **52**, 1252–1264, DOI: [10.1190/1.1442386](https://doi.org/10.1190/1.1442386).
- Gao, S., Liu, H., Davis, P. M. and Knopoff, G. L. (1996): Localized amplification of seismic waves and correlation with damage due to the Northridge earthquake, *Bull. Seis. Soc. Am.*, **86**, 209–230.
- Geli, L., Bard, P. Y. and Beatrice, J. (1988): The effect of topography on earthquake ground motion: a review and new results, *Bull. Seismol. Soc. Am.*, **78**, 42–63.
- Graves, R. W., Pitarka, A. and Somerville, P. G. (1998): Ground motion amplification in the Santa Monica area: Effects of shallow basin edge structure, *Bull. Seismol. Soc. Am.*, **88**, 1224–1242.
- Hallier, S., Chaljub, E., Bouchon, M. and Sekiguchi, H. (2008): Revisiting the basin-edge effect at Kobe during the 1995 Hyogo-Ken Nanbu earthquake, *Pure Appl. Geophys.*, **165**, 1751–1760, DOI: [10.1007/s00024-008-0404-y](https://doi.org/10.1007/s00024-008-0404-y).
- Israeli, M. and Orszag, S. A. (1981): Approximation of radiation boundary conditions, *J. Comput. Phys.*, **41**, 115–135.
- Kamal and Narayan, J. P. (2015): 3D basin-shape-ratio effects on frequency content and spectral amplitudes of basin-generated surface waves and associated spatial ground motion amplification and differential ground motion, *J. Seismol.*, **19**, 293–316, DOI: [10.1007/s10950-014-9466-8](https://doi.org/10.1007/s10950-014-9466-8).
- Kawase, H. (1993): Effects of surface and subsurface irregularities, in: *Earthquake and ground motions*, Part 1, Chapter 3, Architectural Institute of Japan, 118–155.
- Kawase, H. (1996): The cause of damage belt in Kobe: “The basin-edge effect” constructive interference of the direct S-wave with the basin-induced diffracted/Rayleigh waves, *Seism. Res. Lett.*, **67**(5), 25–34, DOI: [10.1785/gssrl.67.5.25](https://doi.org/10.1785/gssrl.67.5.25).
- Kristek, J. and Moczo, P. (2003): Seismic-wave propagation in viscoelastic media with material discontinuities: A 3D fourth order staggered-grid finite-difference modeling, *Bull. Seismol. Soc. Am.*, **93**, 2273–2280, DOI: [10.1785/0120030023](https://doi.org/10.1785/0120030023).
- Kumar, S. and Narayan, J. P. (2008a): Importance of quantification of local site effects based on wave propagation in seismic microzonation, *J. Earth Sci. Syst.*, **117**(S2), 731–748, DOI: [10.1007/s12040-008-0067-1](https://doi.org/10.1007/s12040-008-0067-1).
- Kumar, S. and Narayan, J. P. (2008b): Absorbing boundary conditions in a fourth-order accurate SH-wave staggered grid finite difference algorithm, *Acta Geophysica*, **56**, 1090–1108, DOI: [10.2478/s11600-008-0043-9](https://doi.org/10.2478/s11600-008-0043-9).

- Lee, S. J., Chen, H. W. and Huang, B. S. (2008): Simulations of strong ground motion and 3-D amplification effect in the Taipei basin by using a composite grid finite-difference method, *Bull. Seismol. Soc. Am.*, **98**, 1229–1242, DOI: [10.1785/0120060098](https://doi.org/10.1785/0120060098).
- Lee, J. (2013): Earthquake site effect modeling in the Granada basin using a 3-D indirect boundary element method, *Phys. Chem. Earth*, **63**, 102–115, DOI: [10.1016/j.pce.2013.03.003](https://doi.org/10.1016/j.pce.2013.03.003).
- Moczo, P., Kristek, J., Vavryčuk, V., Archuleta, R. J. and Halada, L. (2002): 3D heterogeneous staggered-grid finite-difference modelling of seismic motion with volume harmonic and arithmetic averaging of elastic moduli and densities, *Bull. Seismol. Soc. Am.*, **92**, 3042–3066.
- Narayan, J. P., Sharma, M. L. and Kumar, A. (2002): A seismological report on the 26 January 2001, Bhuj, India earthquake, *Seismol. Res. Lett.*, **73**, 343–355, DOI: [10.1785/gssrl.73.3.343](https://doi.org/10.1785/gssrl.73.3.343).
- Narayan, J. P. (2005): Study of basin-edge effects on the ground motion characteristics using 2.5-D modeling, *Pure Appl. Geophys.*, **162**, 273–289, DOI: [10.1007/s00024-004-2600-8](https://doi.org/10.1007/s00024-004-2600-8).
- Narayan, J. P. and Kumar, S. (2008): A fourth order accurate SH-wave staggered grid finite-difference algorithm with variable grid size and VGR-stress imaging technique, *Pure Appl. Geophys.*, **165**, 271–294, DOI: [10.1007/s00024-008-0298-8](https://doi.org/10.1007/s00024-008-0298-8).
- Narayan, J. P. (2010): Effects of impedance contrast and soil thickness on the basin transduced Rayleigh waves and associated differential ground motion, *Pure Appl. Geophys.*, **167**, 1485–1510, DOI: [10.1007/s00024-010-0131-z](https://doi.org/10.1007/s00024-010-0131-z).
- Narayan, J. P. (2012): Effects of P-wave and S-wave impedance contrast on the characteristics of basin transduced Rayleigh waves, *Pure Appl. Geophys.*, **169**, 693–709, DOI: [10.1007/s00024-011-0338-7](https://doi.org/10.1007/s00024-011-0338-7).
- Narayan, J. P. and Kumar, V. (2012): Numerical study of effects of synclinal basement topography on ground motion characteristics, in: *Proceedings of 15<sup>th</sup> World Conference on Earthquake Engineering (15WCEE)*, Lisbon, Portugal, September 24–28, Paper No. 3144.
- Narayan, J. P. and Kumar, V. (2014a): Study of combined effects of sediment rheology and basement focusing in an unbounded viscoelastic medium using P-SV-wave finite-difference modelling, *Acta Geophysica*, **62**, 1214–1245, DOI: [10.2478/s11600-013-0199-9](https://doi.org/10.2478/s11600-013-0199-9).
- Narayan, J. P. and Kumar, V. (2014b): A numerical study of effects of ridge-weathering and ridge-shape-ratio on the ground motion characteristics, *J. Seismol.*, **19**, 83–104, DOI: [10.1007/s10950-014-9452-1](https://doi.org/10.1007/s10950-014-9452-1).
- Narayan, J. P. and Sahar, D. (2014): Three-dimensional viscoelastic finite-difference code and modelling of basement focusing effects on ground motion characteristics, *Computat. Geosci.*, **18**, 1023–1047, DOI: [10.1007/s10596-014-9442-y](https://doi.org/10.1007/s10596-014-9442-y).
- Pitarka, A., Irikura, K., Iwata, T. and Sekiguchi, H. (1998) Three dimensional simulation of the near fault ground motion for 1995, Hyogo-ken Nanbu (Kobe), Japan, earthquake, *Bull. Seismol. Soc. Am.*, **88**, 428–440.
- Shiuly, A. and Narayan, J. P. (2012): Deterministic seismic microzonation of Kolkata city, *Natural Hazards*, **60**, 223–240, DOI: [10.1007/s11069-011-0004-5](https://doi.org/10.1007/s11069-011-0004-5).

#### SAŽETAK

### **Kvantifikacija učinaka geometrijskog oblika granične plohe između osnovne stijene i sedimenata u trodimenzionalnom bazenu s kružnom površinom**

*Jay Prakash Narayan i Kamal*

U radu se prezentiraju efekti geometrijskog oblika granične plohe između osnovne stijene i sedimenata (GSBI) u trodimenzionalnom bazenu s kružnom površinom na svo-

jstva i fokusiranje površinskih valova generiranih unutar bazena (BGS), te na s s time povezane prostorne varijacije prosječne spektralne amplifikacije (ASA) i prosječnog faktora pogoršanja (AAF). Povećanje ASA prema središtu polusferičnog bazena (SS-) u usporedbi s dvodimenzionalnim bazenom uzrokuje fokusiranje BGS-valova u SS-bazenu. Iznos ASA 2.8 puta veći u odnosu na 2D bazen, ukazuje na potrebnu pažnju pri procjeni potresne opasnosti u takvim sedimentnim bazenima. Analize simulacija pokazuju da GSBI jako utječe na amplifikaciju amplituda zbog fokusiranja BGS-valova. Na primjer, ASA je na rubu trapezoidalnog bazena s nagibom rubova od  $20^\circ$  50% veća nego u središtu takvog bazena s nagibom od  $45^\circ$ . Pri seizmičkom mikrozoniranju koje je bazirano na 1D-odzivu sedimenata, preporučuje se da se AAF računa koristeći jednake komponente gibanja tla kao i za upadni val, kako bio se konzervativno procijenilo faktor pogoršanja gibanja tla, te kako bi se uključilil 3D-efekti.

*Ključne riječi:* trodimenzionalna simulacija konačnim razlikama, površinski valovi generirani unutar sedimentnog bazena, fokusiranje površinskih valova, faktori pogoršanja i prosječna spektralna amplifikacija

*Corresponding authors' address:* J. P. Narayan and Kamal, Department of Earthquake Engineering, Indian Institute of Technology, Roorkee-247667, India, e-mail: jaypnfeq@iitr.ac.in, kamalbattan@gmail.com